

Optimizing rod-shaped anode configuration in ultra-high-current-density seawater electrolysis for scalable hydrogen production

Søren A. Tornøe ^{a,b}, John W. Koster ^c, Ishan Jain ^d, Andy V. Surin ^{a,b}, Aiden Krauss ^{a,b}, Nobuhiko P. Kobayashi ^{a,b*}

^a Nanostructured Energy Conversion Technology and Research (NECTAR), Department of Electrical and Computer Engineering, Baskin School of Engineering, University of California Santa Cruz, California, 95064, USA

^b Materials Science and Engineering Program, University of California Santa Cruz, California, 95064, USA

^c Ocean Sciences Department, University of California Santa Cruz, California, 95064, USA

^d Eastlake High School, Sammamish, Washington, 98074, USA

Abstract

Growing concern over the environmental impact of fossil fuels has intensified efforts to develop sustainable routes for hydrogen production. Seawater electrolysis powered by renewable energy offers a particularly attractive option because of seawater's abundance and high ionic conductivity. Yet, its progress has been limited by the tendency of the chlorine evolution reaction (CER) to dominate over the oxygen evolution reaction (OER), leading to chlorine generation and associated environmental hazards. In our previous work, we showed that operating at high current densities ($J_c > 10 \text{ A/cm}^2$) with consumable graphite rod-shaped electrodes can effectively suppress CER. Building on that foundation, the present study examines how hydrogen production performance changes with the number and configuration of rod-shaped anodes used with a single cathode. Through a combination of experiments and two-dimensional finite-element modeling, we found that multi-anode configurations can be tuned to enhance hydrogen yield while maintaining full CER suppression. Reducing the electrode spacing from 10 mm to 1 mm increases the local electric field by roughly an order of magnitude, lowering the energy demand from about 980 Wh to 98 Wh per gram of hydrogen. Accounting for field-enhanced ionic mobility—potentially up to eightfold for H^+ ions—further reduces the projected energy cost to near the 50–60 Wh/g H_2 range, approaching the thermodynamic limit. These results demonstrate that electrode geometry and spacing are central to improving both efficiency and scalability in high-current-density seawater electrolysis.

Introduction

The escalating urgency to mitigate the environmental consequences of anthropogenic global warming has intensified global efforts to develop sustainable hydrogen production

technologies.^{1,2} Among these technologies, seawater electrolysis powered by renewable energy sources has emerged as a promising pathway, offering two distinct advantages over freshwater electrolysis: seawater's inherently higher electrical conductivity, which would lower energy demand, and its vast, nearly inexhaustible availability.^{3,4} Despite these benefits, seawater electrolysis faces a persistent challenge—the preferential kinetics of the Chlorine Evolution Reaction (CER) over the Oxygen Evolution Reaction (OER) at the anode.^{5,6,7,8} This preferential kinetics results in the generation of toxic chlorine gas and a cascade of harmful chlorine-derived oxidants, such as hypochlorous acid and hypochlorite ions. Conventional approaches to suppress CER typically rely on nanostructured catalytic coatings that promote OER.^{9,10} However, these methods are often constrained to low operational current densities ($J_c < 1 \text{ A cm}^2$), limiting hydrogen production rates and often relying on catalysts, which hinder scalability and economic feasibility.¹¹ In our previous studies, we introduced a fundamentally different approach to

¹ Turner, J. A. (2004). Sustainable hydrogen production. *Science*, 305, 972. 10.1126/science.1103197

² Sakthivel, S. (2024). Perspectives on CO₂-Free Hydrogen Production: Insights and Strategic Approaches. *Energy & Fuels*, 38, 20033. 10.1021/acs.energyfuels.4c03156

³ Zhang, R., Tingting, Z., Wang, H., & Lu, S. (2024). Recent Advances in High-Performance Direct Seawater Electrolysis for “Green” Hydrogen. *Advanced Energy & Sustainability Research*, 5, 2400085. 10.1002/aesr.202400085

⁴ Sun, J.-P., Zhao, Z., Li, J., Li, Z.-Z., & Meng, X.-C. (2023). Recent advances in electrocatalytic seawater splitting. *Rare Metals*, 42, 751. 10.1007/s12598-022-02168-x

⁵ Harvey, C., Delacroix, S., & Tard, C. (2024). Unraveling the Competition between the Oxygen and Chlorine Evolution Reactions in Seawater Electrolysis: Enhancing Selectivity for Green Hydrogen Production. *Electrochimica Acta*, 497, 144534. 10.1016/j.electacta.2024.144534

⁶ Vos, J. G., Liu, Z., Speck, F. D., Perini, N., Fu, W., Cherevko, S., & Koper, M. T. M. (2019). Selectivity Trends Between Oxygen Evolution and Chlorine Evolution on Iridium-Based Double Perovskites in Acidic Media. *ACS Catalysis*, 9, 8561. 10.1021/acscatal.9b01159

⁷ Raza, N. (2025). Challenges and solutions in suppressing chlorine evolution reaction in seawater electrolysis. *Journal of Power Sources*, 659, 238331. 10.1016/j.jpowsour.2025.238331

⁸ Zhao, C., Ding, Z., Zhang, K., Du, Z., Fang, H., Chen, L., Jiang, H., Wang, M., & Wu, M. (2025). Comprehensive Chlorine Suppression: Advances in Materials and System Technologies for Direct Seawater Electrolysis. *Nano-Micro Letters*, 17, 113. 10.1007/s40820-025-01653-z

⁹ Bahuguna, G., & Patolsky, F. (2024). Routes to Avoiding Chlorine Evolution in Seawater Electrolysis: Recent Perspective and Future Directions. *ACS Materials Letters*, 4, 3202. 10.1021/acsmaterialslett.4c00409

¹⁰ Trasatti, S. (1984). Electrocatalysis in the anodic evolution of oxygen and chlorine. *Electrochimica Acta*, 29(11), 1503. 10.1016/0013-4686(84)85004-5

Turner, J. A. (2004). Sustainable hydrogen production. *Science*, 305, 972. 10.1126/science.1103197

¹¹ Roger, I., Shipman, M. A., & Symes, M. D. (2017). Earth-abundant catalysts for electrochemical and photoelectrochemical water splitting. *Nature Reviews Chemistry*, 1, 0003. doi.org/10.1038/s41570-016-0003

seawater electrolysis, centered on two key innovations: (1) operating at significantly higher current densities ($J_c > 10 \text{ A/cm}^2$) to suppress CER and enhance hydrogen yield, and (2) employing consumable rod-shaped graphite electrodes, chosen for their exceptional corrosion resistance as the most noble material in the Galvanic Series. Using a micro-scale electrolysis system with a 1000 ml seawater capacity and a simplified gas collection mechanism, we demonstrated an electrochemical regime in which reactive chlorine species were substantially minimized, achieving both environmental and economic incentives. We refer to this distinctive technique as high-current-density seawater water electrolysis.^{12,13}

The initial seawater electrolysis systems we developed were, however, constrained to a single pair of rod-shaped electrodes, which restricted our ability to explore and optimize the electrode arrangements expected to be critical for scaling up high-current density seawater electrolysis. Apparently, unlike conventional electrolysis that utilizes a pair of planar-electrodes, in using rod-shaped electrodes. A key advantage of rod-shaped electrodes is that the rod diameter, which defines the effective electrochemically active area, can be independently tuned relative to the nominal electrode gap. This geometric flexibility is not achievable with conventional planar electrode configurations. Furthermore, there exists a vast design space involving numerous variables, including the total number of rod-shaped anodes and cathodes as well as their spatial geometrical arrangements, each potentially exerting significant influence on system performance. Building on these preliminary insights, the current study systematically investigates how hydrogen production varies as a function of the number of rod-shaped anodes paired with a single rod-shaped cathode. This approach is aimed at progressing toward a larger-scale, more efficient seawater electrolysis system by exploring multi-electrode configurations beyond the simple one-to-one pairing. Our working hypothesis postulates that increasing the number of anodes will induce nonlinear changes in key electrochemical properties such as charge transport dynamics and surface reaction kinetics, ultimately affecting both performance and energy efficiency. To test this hypothesis, we conduct a thorough comparative experimental analysis, focusing on how different electrode configurations impact electrical and electrochemical behavior. In particular, we emphasize evaluating the energy consumption required to produce a fixed amount of hydrogen under conditions where CER is fully suppressed, thereby ensuring environmental compatibility. Complementing these experiments, a simple 2D finite-element modeling is performed to provide deeper mechanistic insights into the complex interactions and phenomena observed, enabling a more predictive understanding of high-current-density seawater electrolysis with multiple rod-shaped electrodes.

¹² Koster, J. W., Tornøe, S. A., Kobayashi, N. P., & Potts, D. C. (2023). Explicitly controlling electrical current density overpowers the kinetics of the chlorine evolution reaction and increases the hydrogen production during seawater electrolysis. *International Journal of Hydrogen Energy*, 48, 4994. 10.1016/j.ijhydene.2022.11.053

¹³ Tornøe, S. A., Koster, J. W., Surin, A. V., Sands, J. H., & Kobayashi, N. P. (2025). Seawater electrolysis at ultra-high current density: A comparative analysis of cylindrical versus conical electrodes. *International Journal of Hydrogen Energy*, 114, 9. 10.1016/j.ijhydene.2025.03.003

Experimental Design

The reaction chamber for this experiment remains identical to the lid-off configuration from our previous study¹⁴. The lid off configuration was chosen as testing revealed that when pressurized beyond ambient pressure, the power requirements to reach 10 A/cm² are increased and the electrolysis reaction tends to degrade substantially faster. As such, with the lid off, the system displays a higher starting current and maintains better long-term operational stability. A divergence from the original lid-off configuration is the opposing 3x3 box patterns of holes 2 mm in diameter centered 100 mm from the bottom of the box. Holes are spaced 5 mm center to center from each other. This allows for a variation in the number and configuration of the anodes and cathodes. The four primary configurations we will be going over in this study are depicted in Fig. 1, with Fig. 1a being the base configuration from our last study set at a 10 mm electrode gap. In our previous study the electrode gap was 15 mm, as we were trying to minimize the effects of the side (i.e., cylindrical areas associated with the side of a rod-shaped electrode) of the electrode. However, our modeling indicated that the electrolysis occurring at the side of the electrode was minimal, while increasing the electrode gap increased the overall resistance of the system and consequently reduced the hydrogen production efficacy. As such, for this study, we chose to return to our first study's electrode gap of 10 mm¹⁵. Fig. 1 provides a schematic illustration of the four electrode configurations used in the experiments. In all cases, the electrode gap was fixed at 10 mm between the cathode and the center of the anode assembly. The configurations are: (a) single-anode/single-cathode (1a–1c), (b) split-anode (2a–1c), (c) inverted-delta (3a–1c), and (d) square (4a–1c). Fig. 2 displays schematic diagrams and detailed dimensions of the four electrode configurations. Panels (a–d) show the 1a–1c configuration: (a) top view, (b) side view, (c) view from the anode, and (d) view from the cathode. Panels (e–g) show the 2a–1c configuration: (e) top view, (f) side view, and (g) view from the anode/cathode. Panels (h–j) show the 3a–1c

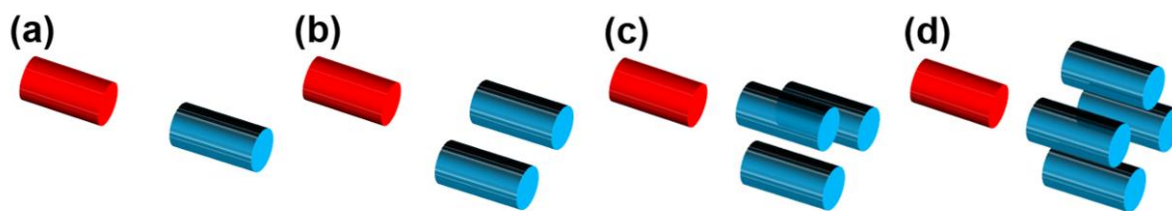


Fig. 1: Schematic illustration of the four electrode configurations used in the experiments. In all cases, the electrode gap was fixed at 10 mm between the cathode and the center of the anode assembly. The configurations are: (a) single-anode/single-cathode (1a–1c), (b) split-anode (2a–1c), (c) inverted-delta (3a–1c), and (d) square (4a–1c).

¹⁴ Tornøe, S. A., Koster, J. W., Surin, A. V., Sands, J. H., & Kobayashi, N. P. (2025). Seawater electrolysis at ultra-high current density: A comparative analysis of cylindrical versus conical electrodes. *International Journal of Hydrogen Energy*, 114, 9. 10.1016/j.ijhydene.2025.03.003

¹⁵ Koster, J. W., Tornøe, S. A., Kobayashi, N. P., & Potts, D. C. (2023). Explicitly controlling electrical current density overpowers the kinetics of the chlorine evolution reaction and increases the hydrogen production during seawater electrolysis. *International Journal of Hydrogen Energy*, 48, 4994. 10.1016/j.ijhydene.2022.11.053

configuration: (h) top view, (i) side view, and (j) view from the anode/cathode. Panels (k–m) show the 4a–1c configuration: (k) top view, (l) side view, and (m) view from the anode/cathode. The unit is mm.

The electrodes used in this study remain the same as our previous study; 2.0 mm diameter June Gold 4B graphite lead with the flat cylindrical ends used as the electrode faces. Using a 3D printed gap setting tool, the electrodes were set to protrude into the reaction chamber by 5 mm. The gas collection apparatus for this study has also been further refined using a 3D printed gas separator in place of our previous barrier. The separator was designed and printed out of PETG to separate the forming anodic and cathodic gases from each other while funneling the cathodic (i.e., hydrogen) gas towards our collection vessel with minimal to no loss of cathodic gas. The apparatus was printed on a PRUSA XL using a 0.4 mm nozzle and a 0.25 mm layer height with nozzle and bed temperatures of 250C and 80C, respectively. The collection vial itself has also been improved with an expanded volume and graduation marks, negating some of the complexity and further improving the accuracy of the previous measurement system. A single Matrix Technology Inc. WPS300S-150-5 (150V/5A/300W) programmable DC power supply operated in constant-current mode was used to power the various electrode configurations. The anode(s) were individually powered using equal-length 1.2 m wire leads (16 AWG, E Insulation, SPC Conductor Material, 19/29 Strand, with alligator clips) connected to the portion of the electrodes external to the reaction chamber. Leads were connected flush to the chamber walls to maintain equal lengths between each of the individually connected electrodes. The duration of each trial was 120 seconds.

In our previous study, we demonstrated that maintaining a minimum system current density (J) of 10 A/cm² effectively suppresses CER^{16,17}, and results in an average hydrogen production rate of 15 ml/min. To minimize the number of variables that may have an impact on our system's behavior, we decided to operate using the same conditions as in our previous study. For the present study, this amounts to an electrode gap of 10 mm, and a constant 10 A/cm² across the cathode, as the number of anodes was systematically varied from one to four, while the number of cathodes remained fixed to one. This allowed us to directly observe the effects of changing only the anodic electrode configurations. As a result, electrode configurations besides the typical one anode-one cathode (1a-1c) will not be running the anodes at 10 A/cm², which again was done intentionally to better observe how the configurations affect the behavior of the system. Thus, 10 A/cm² was maintained at the single cathode in each of the four electrode configurations. Our previous studies on the 1a-1c configuration revealed that under such high J conditions, the anode undergoes significant morphological modification and loss

¹⁶ Koster, J. W., Tornøe, S. A., Kobayashi, N. P., & Potts, D. C. (2023). Explicitly controlling electrical current density overpowers the kinetics of the chlorine evolution reaction and increases the hydrogen production during seawater electrolysis. *International Journal of Hydrogen Energy*, 48, 4994. 10.1016/j.ijhydene.2022.11.053

¹⁷ Tornøe, S. A., Koster, J. W., Surin, A. V., Sands, J. H., & Kobayashi, N. P. (2025). Seawater electrolysis at ultra-high current density: A comparative analysis of cylindrical versus conical electrodes. *International Journal of Hydrogen Energy*, 114, 9. 10.1016/j.ijhydene.2025.03.003

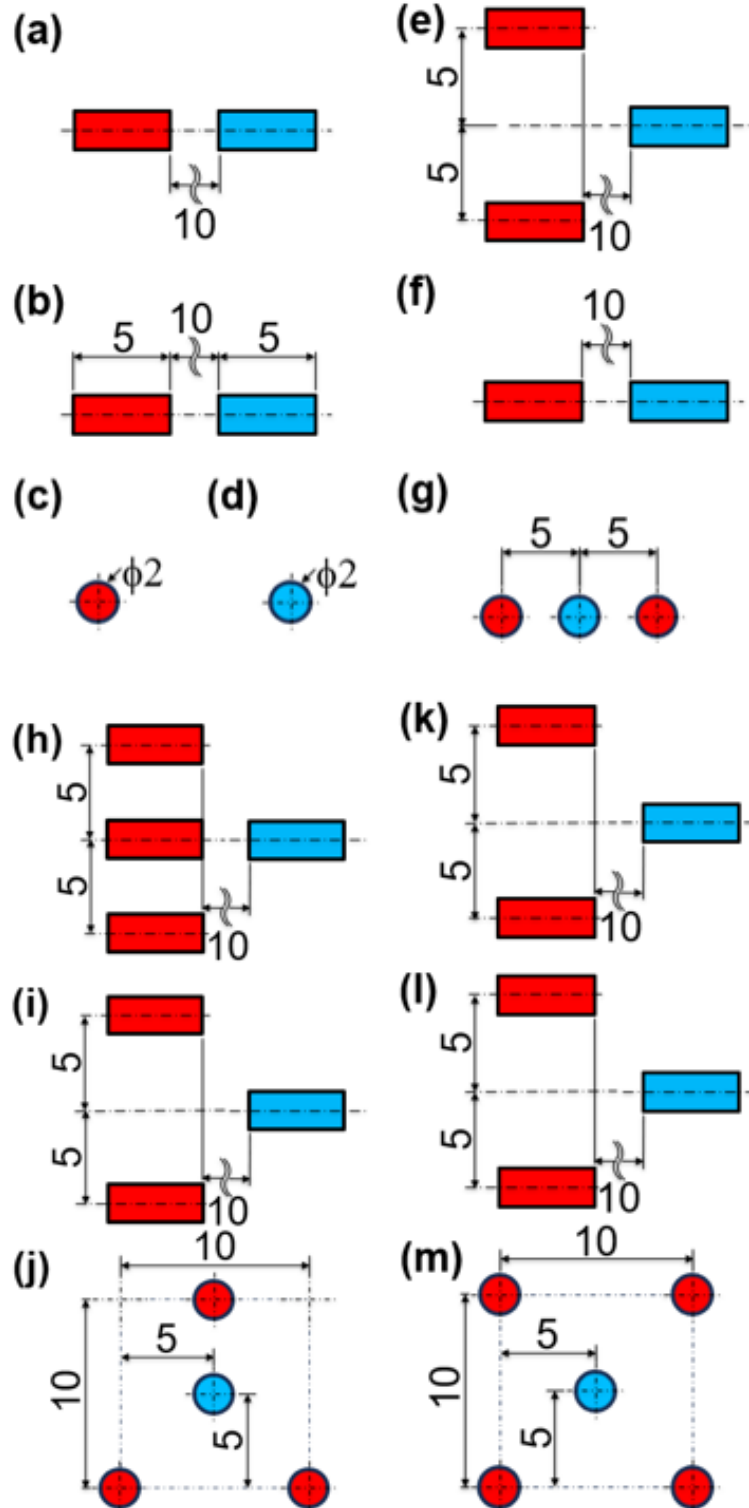


Fig. 2: Schematic diagrams and detailed dimensions of the four electrode configurations. Panels (a–d) show the 1a–1c configuration: (a) top view, (b) side view, (c) view from the anode, and (d) view from the cathode. Panels (e–g) show the 2a–1c configuration: (e) top view, (f) side view, and (g) view from the anode/cathode. Panels (h–j) show the 3a–1c configuration: (h) top view, (i) side view, and (j) view from the anode/cathode. Panels (k–m) show the 4a–1c configuration: (k) top view, (l) side view, and (m) view from the anode/cathode. The unit is mm.

throughout the electrolysis period. This negatively impacts the system by reducing the operational lifetime of a set of electrodes and adds more frequent downtime for replacement of consumables, which is not ideal in an industrial scale system. Consequently, the present electrode configurations were designed to distribute the total current among multiple anodes, thereby reducing the current load applied to each individual anode while maintaining the overall current density at $J = 10 \text{ A/cm}^2$ through the single cathode. This approach enables the mitigation of localized anode degradation without compromising the desired higher J electrochemical operating regime at the cathode. Certain anode configurations also have the potential to reduce CER by creating chloride depletion regions between the active areas of the anodes – active areas being the portions of the anodes that face the cathode (i.e., those portions of the electrodes that are closest in terms of their direct paths). With regard to testing multi-cathode configurations – which we are not addressing in this study – we experimented with it briefly, only to confirm that the system scales linearly in symmetric anode-cathode configurations (i.e., 2a-2c produces 30ml/min but at double the current for the same voltage). For the case of a singular anode held at 10 A/cm^2 with varying numbers of cathodes will also not be addressed in this study as increasing the number of cathodes both speeds up the morphological modifications to the anode and via Faraday's laws of electrolysis would not improve hydrogen production rates. Additionally, the results encountered in this study are expected to scale up linearly. That is to say, that the results of a 2a-1c configuration is expected to behave the same as a 4a-2c configuration, but at double the power consumption. As a result, we have decided to only concern ourselves with the base case of only one cathode.

Results and Discussion

Fig. 3a presents the current–voltage (I–V) characteristics of the electrolyzer for the four electrode configurations. The applied anode voltage V_A was swept from 0 to 60 V, and the corresponding current response was measured. The 1a-1c configuration (red) is clearly distinct from the others, showing substantially lower current at, in particular, voltages above 40 V. The I–V curve of the 1a-1c configuration exhibits a reduced slope, corresponding to lower electrical conductance, and it appears to begin to approach saturation as the voltage increases, with the current leveling off near 60 V. This behavior suggests that the 1a-1c configuration imposes a significant limitation on charge transport during electrolysis. By contrast, the 2a-1c configuration (cyan) demonstrates improved conductance, with an approximately linear current rise up to ~60 V. The 3a-1c (orange) and 4a-1c (blue) configurations show nearly overlapping I–V responses across the entire voltage range, with both producing substantially higher current than the 1a-1c configuration. The close overlap indicates that once three or more anodes are introduced, the current pathways and effective electric field distribution may be optimized to some extent, leading to a near-saturation in improvement on electrical conductance. A slight enhancement for the 4a-1c configuration over the 3a-1c case can still be observed, suggesting incremental but diminishing benefits from further increasing the number of anodes. Overall, the results highlight that increasing the number of anodes significantly enhances electrical conductance up to a point, with drastically diminishing returns beyond three anodes.

Fig. 3b presents the differential conductance (dI/dV) as a function of applied voltage V_A for the four electrode configurations: 1a-1c (red), 2a-1c (cyan), 3a-1c (orange), and 4a-1c (blue). These curves are derived from the current-voltage characteristics shown in Fig. 3a. Overall, the 1a-1c configuration maintains a nearly constant dI/dV over a wide voltage range, while the others exhibit linear characteristics, with 3a-1c and 4a-1c achieving the highest dI/dV . Across all configurations, a clear onset of conductance is observed near 2 V, followed by a rapid increase in dI/dV , indicating the presence of a transition into a regime where the conductance stabilizes, forming a plateau that persists over a certain voltage range. The 1a-1c configuration exhibits the lowest dI/dV among all configurations. After the initial rise, dI/dV of the 1a-1c configuration enters a plateau region at $dI/dV \sim 3.3 \times 10^{-2}$ A/V spanning approximately 10 V to 50 V. Beyond ~ 50 V, a noticeable drop in dI/dV occurs, indicating a diminishing rate of current increase with voltage. The 2a-1c configuration (cyan) shows a similar initial trend to the 1a-1c configuration but offset upward by $\sim 15 \times 10^{-2}$ A/V. For the 2a-1c configuration, the dI/dV plateau region is centered around $dI/dV \sim 4.5 \times 10^{-2}$ A/V and extends from ~ 10 V to ~ 20 V. Unlike the 1a-1c configuration, dI/dV of the 2a-1c configuration does not exhibit a significant drop-off within the voltage range examined. The 3a-1c configuration (orange) demonstrates a higher dI/dV plateau region at $dI/dV \sim 5.3 \times 10^{-2}$ A/V from ~ 10 V to ~ 25 V. The 3a-1c configuration introduces distinctive oscillatory behavior in dI/dV , suggesting voltage-dependent

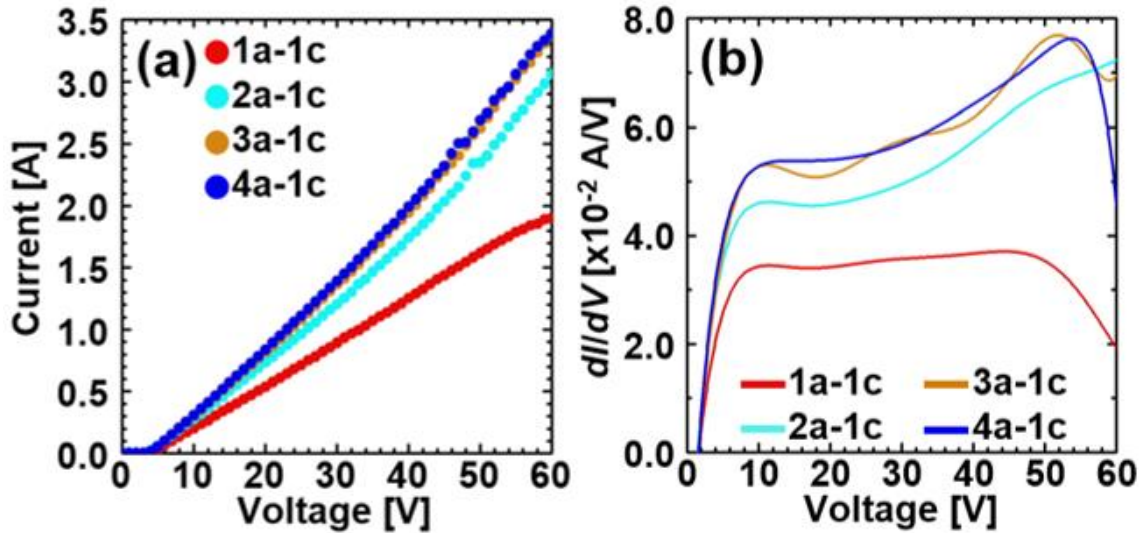


Fig. 3: Panel (a) Current–voltage (I – V) characteristics of the electrolyzer for four electrode configurations. The anode voltage V_A was swept from 0 to 60 V while measuring the current. The 1a–1c configuration shows the lowest current and a tendency toward saturation, whereas 2a–1c exhibits improved, nearly linear behavior. The 3a–1c and 4a–1c configurations yield similar, significantly higher currents, indicating that three or more anodes effectively enhance charge transport and field distribution. Panel (b) Differential conductance (dI/dV) as a function of applied voltage (V_A) for the four electrode configurations. The curves, derived from the current–voltage characteristics in Fig. 1, show a conductance onset near 2 V followed by plateau regions whose magnitude and shape depend strongly on the electrode configuration. While 1a–1c exhibits the lowest and most stable dI/dV , the 3a–1c and 4a–1c configurations reach the highest conductance values, highlighting configuration-dependent charge transport behavior.

fluctuations in the charge transport mechanism. A drop-off is observed beyond ~55 V for the 3a-1c configuration. The 4a-1c configuration (blue) closely mirrors the behavior of the 3a-1c configuration in terms of the magnitude of dI/dV and voltage range, but without the oscillations. The 4a-1c configuration shows a decline in dI/dV at higher voltages. These trends highlight the influence of electrode configuration on charge transport properties.

The oscillatory behavior observed in the 3a-1c configuration may be linked to the dynamics of gas bubbles generated at the anode.^{18,19} These bubbles undergo nucleation, growth, and periodic detachment cycles. While a bubble remains adhered to the electrode surface, it effectively reduces the active conductive area, causing a change in resistance; upon detachment, a sudden increase in conductance is observed. However, this bubble-induced mechanism does not appear to differ significantly between the oscillatory 3a-1c and the non-oscillatory 4a-1c configurations; thus, the oscillatory behavior is unlikely to be solely caused by gas bubbles. Apart from gas bubbles, both 3a-1c and 4a-1c configurations can be categorized as symmetric “cage” structures, yet their localized ionic environments may behave differently. Specifically, the processes of ion depletion and mass transport limited replenishment near the electrodes, these “cage effects” in our electrolysis are a unique feature associated with the configuration of our rod-shaped electrodes that could vary substantially between these two configurations, resulting in periodic fluctuations in conductivity and/or reaction rates seen exclusively in the 3a-1c configuration. Furthermore, localized heating effects are expected to modulate electrical conductivity.^{20,21} Should these thermal effects couple with convective cooling to form a feedback loop, the resulting dynamic interplay—modulated by the spatial arrangement of multiple electrodes—could give rise to the observed oscillatory conductance.²²

Fig. 4 presents the temporal evolution of the voltage required to sustain a constant current density of 10 A/cm² for four electrode configurations during a 60 s hydrogen collection period. In all cases, the operating voltage decreases gradually with time, reflecting a ~5% reduction relative to the initial value, with each additional anode configuration showing a slight further improvement. A clear dependence on the number of anodes is observed:

¹⁸ Ross, B., Haussener, S., & Brinkert, K. (2015). Impact of Gas Bubble Evolution Dynamics on Electrochemical Reaction Overpotentials in Water Electrolyser Systems. *The Journal of Physical Chemistry C*, 129, 4383. 10.1021/acs.jpcc.5c00220

¹⁹ Kuge, T., Nishimoto, T., Kurohagi, M., Maeda, K., Yae, S., & Mukouyama, Y. (2020). Mechanism of Potential Oscillation during Electrolysis of Water in Acidic Solutions. *Electrochemistry*, 88, 157. 10.5796/electrochemistry.19-00065

²⁰ Jacobs, T. S., Park, S., Schöning, M., Weckhuysen, B. M., Koper, M. T. M., & Stam, W. v. d. (2024). Luminescence Thermometry Probes Local Heat Effects at the Platinum Electrode Surface during Alkaline Water Electrolysis. *ACS Energy Letters*, 9, 3335. 10.1021/acsenenergylett.4c01238

²¹ Eichner, B. J., Amiri, M. N., Burheim, O. S., & Lamb, J. J. (2024). 2D simulation of temperature distribution within large-scale PEM electrolysis stack based on thermal conductivity measurements. *Frontiers in Chemical Engineering*, 6, 01. 10.3389/fceng.2024.1384772

²² Xu, N., Qiu, B., Ji, T., Liu, Z., & Chu, H. (2024). Effect of heat and bubble mass transfer on the efficiency of alkaline electrolysis hydrogen production. *Nano Research*, 17, 9345. 10.1007/s12274-024-6922-9

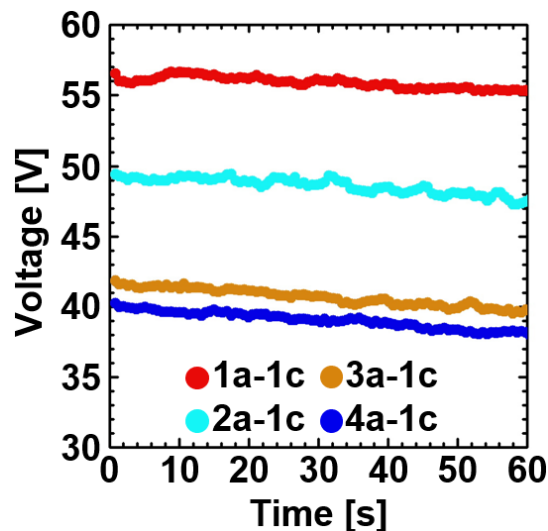


Fig. 4: Voltage evolution at 10 A/cm² over 60 s for four electrode configurations. Increasing anodes lowers steady-state voltage, with diminishing returns beyond three anodes, reducing the required voltage by >15 V. Minor spikes reflect local graphite inhomogeneities. Data was used to estimate energy consumption for producing 1 g of hydrogen.

the steady-state voltage level systematically decreases as additional anodes are introduced. The reduction is most pronounced when moving from the 1a–1c to the 2a–1c configurations as well as from the 2a–1c to 3a–1c configurations. The incremental benefit diminishes at higher anode counts, in particular, the difference between the 3a–1c configuration and 4a–1c configurations is considerably smaller than the earlier transitions, suggesting diminishing returns in voltage reduction beyond three anodes. Overall, increasing the number of anodes from one to four lowers the required voltage by more than 15 V, corresponding to a substantial decrease in energy demand. Minor voltage fluctuations, evident as spikes in the traces, are attributed to local inhomogeneities in the composition of graphite electrodes. The voltage–time characteristics obtained here were further used to calculate the energy consumption associated with generating 1 g of hydrogen.

Fig. 5 presents the energy consumption for producing 1 gram of hydrogen across the four electrode configurations, as indicated along the x-axis by the number of anodes. A pronounced inverse correlation is evident, with energy consumption decreasing from approximately 1.41 kWh in the 1a–1c configuration to about 0.98 kWh in the 4a–1c configuration. This trend clearly demonstrates that increasing the number of anodes contributes to improved energy efficiency. However, the rate of decrease in energy consumption exhibits a diminishing return with each additional anode, suggesting a nonlinear relationship. It is noteworthy that the energy consumption for the 4a–1c configuration, at roughly 0.98 kWh per gram of hydrogen, remains significantly higher

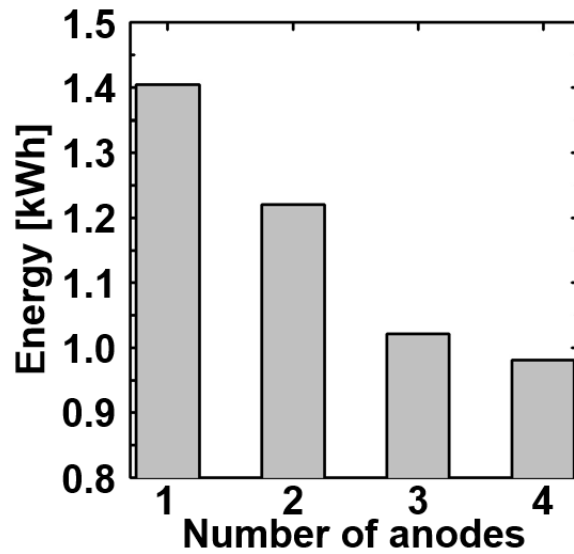


Fig. 5: Energy consumption per gram of hydrogen for four electrode configurations, shown along the x-axis by the number of anodes. Energy decreases from ~1.41 kWh (1a–1c) to ~0.98 kWh (4a–1c), highlighting improved efficiency with additional anodes. The decrease in exhibits diminishing returns, indicating a nonlinear trend.

than the commonly referenced benchmark of approximately 50~60 Wh.^{23,24} This discrepancy will be critically examined in subsequent sections, where we outline strategies to enhance efficiency and approach more optimal performance levels.

Fig. 6 presents a detailed schematic of the top view of the electrolyzer model employed for simulations of electrical potential and electric field distribution. The setup features a seawater-filled rectangular container measuring 100 mm by 40 mm, with a central electrode gap that distinctly separates the anode on one side from the cathode on the other. Situated between these electrodes is a gas separator, characterized by a 10 mm diameter aperture, which serves the dual purpose of preventing mixing of gases generated at the electrodes while enabling ionic conduction through the seawater medium. The gas separator has a uniform thickness of 1.1 mm. This arrangement delineates the spatial domain utilized for modeling the electric potential profile and resultant electric field within the electrolyzer system. Further methodological details and

²³ Glenk, G., & Reichelstein, S. (2019). Economics of converting renewable power to hydrogen. *Nature Energy*, 4, 216. 10.1038/s41560-019-0326-1

²⁴ Lamy, C. (2016). From hydrogen production by water electrolysis to its use in fuel cells. *International Journal of Hydrogen Energy*, 41, 15415. 10.1016/j.ijhydene.2016.04.173

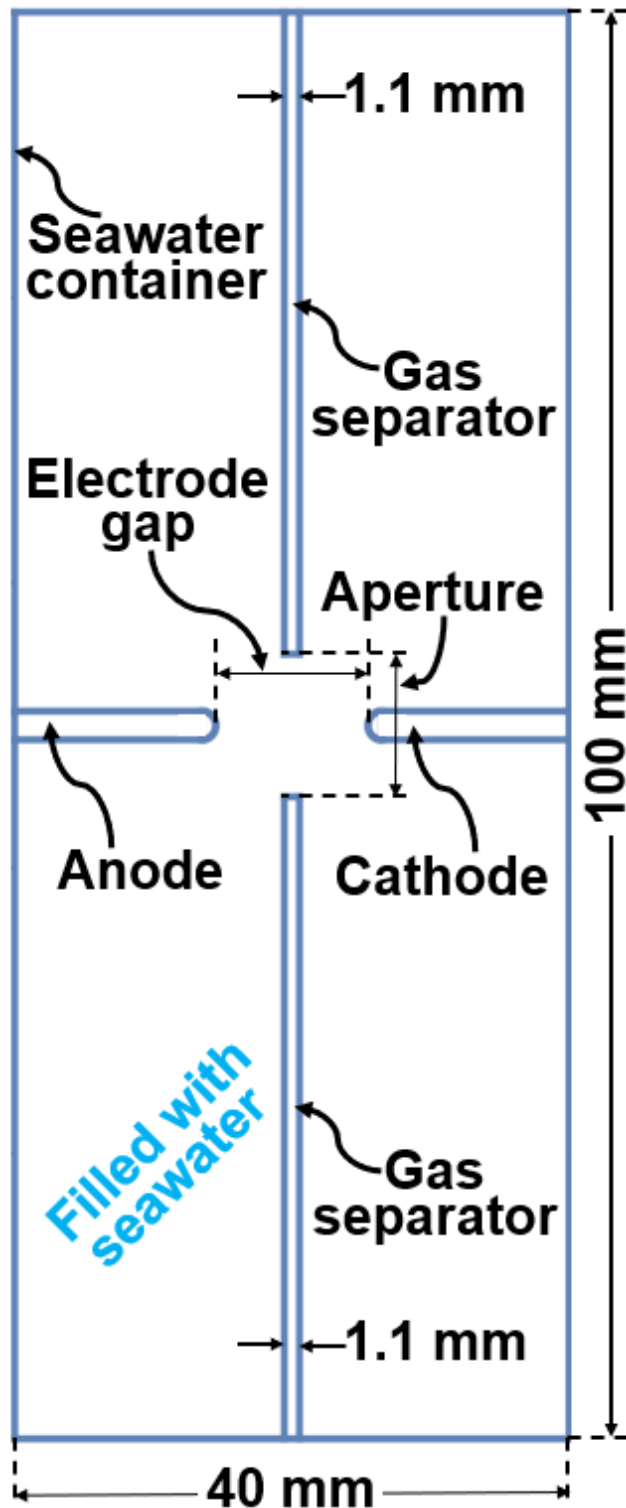


Fig. 6: Top-view schematic of the seawater electrolyzer used for simulations of electric potential and field in the 1a–1c configuration. A 1.1 mm-thick gas separator with a 10 mm aperture separates the anode (40 V) and cathode (ground), allowing ionic conduction while preventing gas mixing. This setup highlights the fundamental effects of electrode gap reduction, with insights applicable across all four configurations studied.

simulation specifically addresses the 1a-1c configuration, wherein a voltage of 40 V is applied to the anode (V_A), while the cathode is maintained at ground potential. The selection of the 1a-1c configuration reflects an intentional simplification to isolate and clarify the fundamental effects associated with electrode gap reduction, eliminating other parasitic influences inherent in more complex configurations. Although the applied voltage V_A of 40 V does not reach the threshold required to sustain a current density of 10 A/cm² in the experimental setup, the derived insights and characteristic behaviors are expected to hold broadly across the four electrode configurations experimentally investigated in this study.

Figs. 7a and 7b illustrate a comparative analysis of the electrical potential distribution between two electrode pairs subjected to the same applied voltage bias of $V_A = 40$ V, but differing significantly in electrode gap—10 mm in panel (a) and a reduced 1 mm gap in panel (b). In the case of the 10 mm electrode gap (panel a), the potential gradient changes gradually across the inter-electrode space, being visually represented by the smooth, continuous color transition ranging from a high potential of 40 V (depicted in red) on the anode side, tapering to 0 V (blue) at the cathode. The equipotential contours are broadly spaced, signifying a relatively weak and uniform electric field intensity within the central region of the electrode gap. Conversely, the 1 mm electrode gap configuration (panel b) displays a markedly steeper potential drop. The voltage transition across the electrodes is abrupt, evidenced by tightly packed color bands. Equipotential lines in this narrower gap are compressed near the electrode edges. Additionally, enhanced fringing effects are

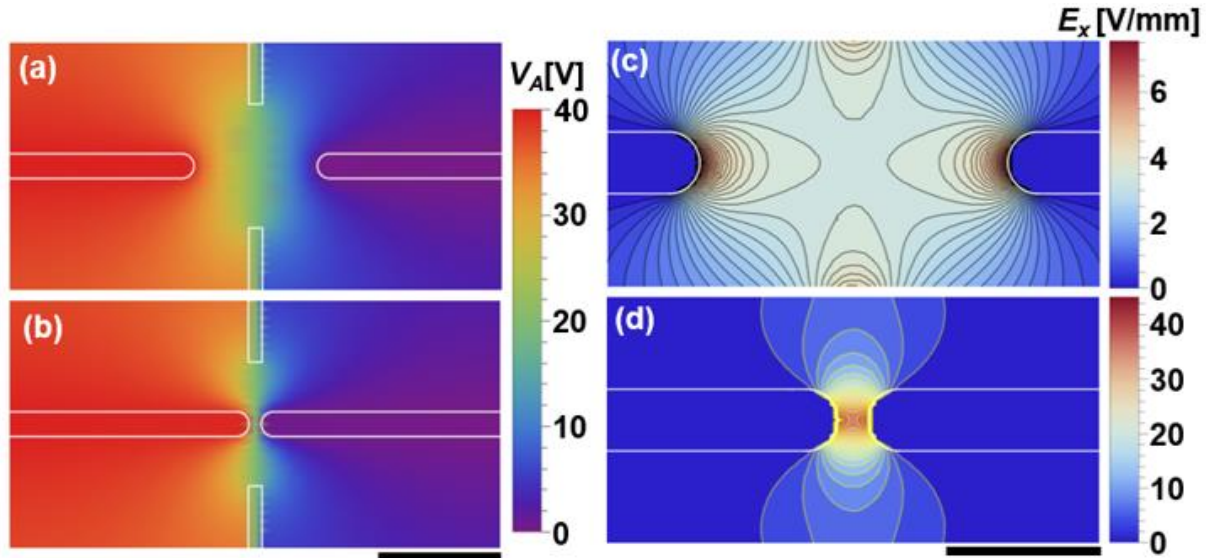


Fig. 7: Electrical potential distribution between two electrode pairs at an applied voltage of $V_A = 40$ V: Panel (a) 10 mm gap, showing a gradual potential drop with smoothly spaced equipotential lines and a relatively uniform field; Panel (b) 1 mm gap, exhibiting a steep potential drop, compressed equipotential lines, and pronounced edge fringing effects. Color scales range from 0 V (blue) to 40 V (red). Scale bar: 10 mm. Spatial distribution of the x-component of the electric field, E_x , under an applied voltage of $V_A = 40$ V for two electrode gaps: 10 mm in Panel (c) and 1 mm in Panel (d). In the 10 mm gap, the field is weak and diffuse (~ 4 V/mm at the center), with broadly spaced lines indicating a gradual potential drop. In contrast, the 1 mm gap produces a strongly localized and intensified field (~ 40 V/mm) near the electrode edges, with dense contours showing pronounced confinement. Scale bar: 5 mm.

observable near the electrode tips, indicative of intensified edge effects common in micro-scale electrode geometries. The scale bar shown corresponds to 10 mm.

Figs. 7c and 7d illustrate the spatial distribution of the x -component of the electric field, E_x , under an applied voltage of $V_A = 40$ V for two electrode gap configurations: 10 mm in panel (c) and 1 mm in panel (d). In the 10 mm gap scenario (panel c), the electric field is relatively diffuse and weak, with the magnitude at the middle of the electrode gap reaching approximately 4 V/mm. The electric field lines are broadly spaced, indicating a gradual potential drop across the larger electrode spacing. While localized field enhancements occur near the electrode edges, the overall field intensity within the inter-electrode region remains modest. This distribution results in a low field gradient through the central gap, suggesting a relatively uniform exposure of the volume between electrodes to the electric field. Conversely, panel (d) with a 1 mm gap reveals a dramatically different field profile. The electric field strength escalates significantly, peaking near 40 V/mm — more than an order of magnitude increase compared to the wider gap. The field is tightly confined and strongly concentrated near the electrode edges and within the narrow gap. This localization is clearly depicted by the densely packed contour lines. Beyond the immediate vicinity of the gap, the field intensity rapidly diminishes, underscoring a pronounced confinement of the electric field around the electrodes. This comparison highlights the critical impact of electrode spacing on electric field distribution and magnitude. Reducing the gap by a factor of ten results in substantial field intensification. The scale bar corresponds to 5 mm.

Fig. 8 illustrates the relationship between the x -component of the electric field, E_x , and the electrode gap. Fig. 8 reveals a pronounced inverse correlation: as the electrode gap increases, E_x decreases systematically. In the narrow gap region up to approximately 2 mm, E_x exhibits a steep decline, underscoring a zone of heightened sensitivity where

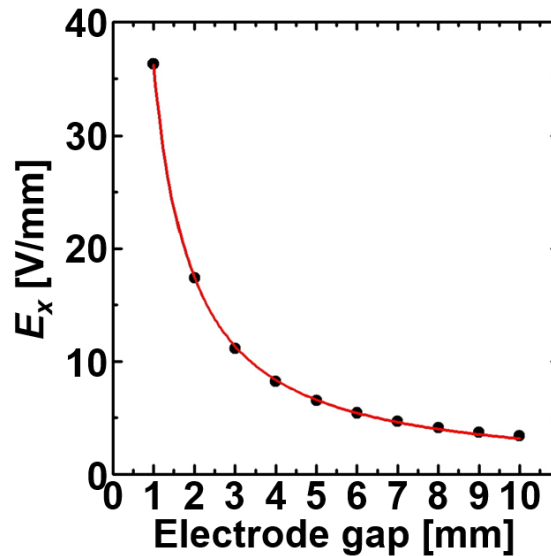


Fig. 8: Dependence of E_x on the electrode gap. E_x decreases sharply for gaps up to ~2 mm, highlighting a region of high sensitivity where small changes in gap significantly alter the field. Beyond ~5 mm, E_x plateaus, indicating reduced sensitivity at larger gaps. The nonlinear trend reflects the interplay between electrode geometry and field distribution.

small adjustments in electrode gap lead to substantial changes in E_x . This sharp drop highlights the crucial role of precise electrode gap in controlling localized electric fields. Beyond roughly 5 mm, the curve plateaus, indicating diminishing returns in field reduction with further increases in gap distance. In this regime, E_x varies more gradually, suggesting reduced sensitivity of the electric field to the electrode gap at larger gaps. This nonlinear behavior reflects the complex interplay between electrode geometry and spatial distribution of the electric field.

Experimentally, the nominal electrode gap was fixed at 10 mm for all four electrode configurations, resulting in, as seen in Fig. 5, an energy consumption of approximately 0.98 kWh to generate 1 gram of hydrogen using the 4a-1c configuration—substantially higher than the often-cited benchmark of 50~60 Wh. However, Fig. 8 clearly suggests that this energy requirement could be markedly lowered by simply reducing the electrode gap. For example, decreasing the gap from 10 mm to 1 mm could theoretically increase E_x by a factor of 10, which would proportionally reduce the voltage needed to sustain a current density of 10 A/cm² by the same factor. Consequently, the energy consumption for hydrogen production using the 1a-1c configuration could be lowered from 0.98 kWh to approximately 98 Wh. Moreover, ionic mobility of key species such as H⁺ in seawater is known to increase nonlinearly with electric field strength. Prior studies report mobility enhancements up to a factor of ~8 for a tenfold increase in the electric field²⁷ and even much higher enhancements, in particular, were reported for anions such as OH⁻ and Cl⁻.²⁸ Applying this scaling to our system—where the local electric field may reach as high as 40 V/mm at a 1 mm gap compared to ~4 V/mm at a 10 mm gap—suggests that energy consumption could be reduced even further, potentially falling well below 50~60 Wh for the production of 1 g of hydrogen. This trend approaches the thermodynamic limit (~40 Wh), though it is important to acknowledge that higher electric fields may also introduce additional loss mechanisms in electrolysis.

Fig. 9 presents the normalized differential electrical conductance (dI/dV , as defined in Fig. 3b) as a function of the number of anodes for four applied voltages: 10, 20, 30, and 40 V. The dashed curves connect experimental data points normalized to the dI/dV value at 10 V for each anode configuration. The solid green curve corresponds to the normalized dI/dV predicted by a simplified resistance-based model (R-mod), in which each cathode is represented by a resistor of resistance R and the collective resistance of n anodes is expressed as R/n , resulting in a total resistance of $R + R/n$ for an $na-1c$ ($n = 1, 2, 3, 4$) configuration. At low applied voltages (10 and 20 V), the experimental trends closely follow the R-mod prediction, indicating that the overall conductance behavior is primarily governed by the geometric scaling of resistive elements. As the applied voltage increases

²⁷ Murad, S. (2011). The role of external electric fields in enhancing ion mobility, drift velocity, and drift-diffusion rates in aqueous electrolyte solutions. *The Journal of Chemical Physics*, 134, 114504. 10.1063/1.3565478

²⁸ Dan, L., Zhang, K., Huang, Z., Wang, F., Wang, Q., & Li, J. (2021). Molecular-level evaluation of ionic transport under external electric fields in biological dielectric liquids. *Journal of Molecular Liquids*, 340, 116883. 10.1016/j.molliq.2021.116883

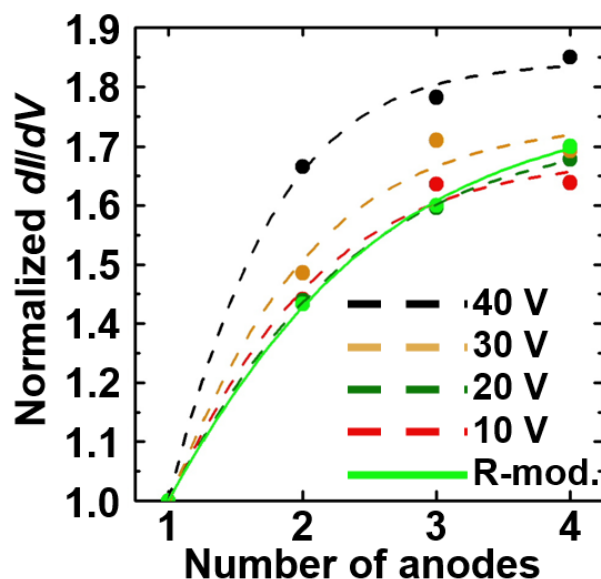


Fig. 9: Normalized differential conductance (dl/dV) vs. number of anodes for 10–40 V. Dashed lines: experimental data normalized to 10 V. Solid green: resistance-model prediction (R-mod). Low-voltage data follow R-mod, while deviations at 30–40 V indicate nonlinear effects such as enhanced ionic mobility and interfacial charge transfer.

to 30 and 40 V, the normalized dl/dV curves progressively deviate upward from the R-mod prediction, suggesting the emergence of nonlinear physicochemical effects such as enhanced ionic mobility and interfacial charge-transfer processes at elevated electric fields.

Conclusion and Future Work

Our initial seawater electrolysis systems, based on a single pair of rod-shaped electrodes, offered key insights but were limited in exploring the broader design space essential for scaling high-current-density seawater electrolysis. Unlike planar electrodes, rod-shaped configurations introduce multidimensional variables—such as electrode count, geometry, and spatial arrangement—that critically influence electrochemical performance. This study systematically examined how hydrogen production scales with the number of rod-shaped anodes paired with a single cathode. Experimental results revealed that multi-anode configurations can be strategically optimized to suppress CER while enhancing hydrogen yield. Reducing the electrode gap from 10 mm to 1 mm could increase the local electric field by an order of magnitude, lowering the required voltage and reducing energy consumption from ~980 Wh to ~98 Wh per gram of hydrogen. When accounting for field-enhanced ionic mobility—potentially up to $8\times$ for H^+ ions—energy requirements may fall below the 55 Wh benchmark assuming 70 % energy efficiency, approaching the thermodynamic limit (approximately $\Delta G = 237.1 \text{ kJ/mol} / 2.016 \text{ g/mol} = \sim 117.6 \text{ kJ} = \sim 32.7 \text{ Wh}$), though high-field losses must be considered. These findings highlight the critical role of electrode configuration and electrode gap optimization in advancing scalable, energy-efficient high current-density seawater electrolysis. Future work should explore complex 3D electrode geometries, dynamic spacing strategies, and durable materials to further improve performance and long-term stability, paving the way toward practical, sustainable hydrogen fuel production using high current-density seawater electrolysis.